JOURNAL OF COMPUTATIONAL PHYSICS 118, 329–347 (1995)

Simulation of Cavity Flow by the Lattice Boltzmann Method

SHULING HOU AND QISU ZOU

Center for Nonlinear Studies and Theoretical Division, Los Alamos National Laboratory, Los Alamos, New Mexico 87545 and Kansas State University, Manhattan, Kansas 66506

SHIYI CHEN

Center for Nonlinear Studies and Theoretical Division, Los Alamos National Laboratory, Los Alamos, New Mexico 87545 and IBM Research Division, T.J. Watson Research Center, P.O. Box 218, Yorktown Heights, New York 10598

GARY DOOLEN

Center for Nonlinear Studies and Theoretical Division, Los Alamos National Laboratory, Los Alamos, New Mexico 87545

AND

ALLEN C. COGLEY

Department of Mechanical Engineering, Kansas State University, Manhattan, Kansas 66506

Received December 2, 1993; revised November 9, 1994

A detailed analysis is presented to demonstrate the capabilities of the lattice Boltzmann method. Thorough comparisons with other numerical solutions for the two-dimensional, driven cavity flow show that the lattice Boltzmann method gives accurate results over a wide range of Reynolds numbers. Studies of errors and convergence rates are carried out. Compressibility effects are quantified for different maximum velocities and parameter ranges are found for stable simulations. The paper's objective is to stimulate further work using this relatively new approach for applied engineering problems in transport phenomena utilizing parallel computers.

1. INTRODUCTION

Lattice gas automata (LGA) and its later derivative, the lattice Boltzmann equation method (LBE), are relatively new approaches that utilize parallel computers to study transport phenomena. Since the first two-dimensional model representing incompressible Navier–Stokes equations was proposed by Frisch, Hasslacher, and Pomeau (FHP) in 1986 [1], LGA have attracted much attention as promising methods for solving a variety of partial differential equations and modeling physical phenomena [2–5].

A lattice gas automaton is constructed as a simplified, fictitious microworld in which space, time, and particle velocities are all discrete. In general, a lattice gas automaton consists of a regular lattice with particles residing on the nodes. A set of Boolean variables $n_i(\mathbf{x}, t)$ $(i = 1, ..., b)$ describing the particle occupation is defined, where b is the number of directions of the particle velocities at each node. Starting from an initial state, the configuration of particles at each time step evolves in two sequential steps: (a) streaming, where each particle moves to the nearest node in the direction of its velocity; and (b) colliding, which occurs when particles arriving at a node interact and possibly change their velocity directions according to scattering rules. For simplicity, the exclusion principle (no more than one particle is allowed at a given time and node moving in a given direction) is imposed for memory efficiency and leads to a Fermi–Dirac equilibrium distribution. The strategy of the lattice gas is twofold: (a) to construct a model as simple as possible of the microworld to permit simulations of a system composed of many particles and (b) to capture the essential features of real collision processes between particles such that, for long times and large scales, macroscopic transport phenomena are captured.

That the evolution of particles on an artificial lattice can simulate the macroscopic behavior of fluid flow is based on the following observations: the macro-dynamics of a fluid is the result of the collective behavior of many particles in the system and details of the microscopic interactions are not essential. Changes in molecular interactions affect transport properties such as viscosity, but they do not alter the basic form of the macroscopic equations as long as the basic conservation laws and necessary symmetries are satisfied [2, 3].

Due to the microscopic nature and local interaction between particles, the lattice gas approach possesses some unique advan-

0021-9991/95 $6.00

tages. The scheme is absolutely stable; boundary conditions are easy to implement; the model is ideal for massively parallel computing because the updating of a node only involves its nearest neighbors, the code is simple and can be easily written in the form for parallel processing. The lattice gas method also contains some problems such as non-Galilean invariance (due to the existence of a density-dependent coefficient in the convection term of the Navier–Stokes equation), an unphysical velocity-dependent pressure, and an inherent statistical noise that requires a spatial or time averaging to obtain smooth macroscopic quantities. To avoid some of these inherent problems, several lattice Boltzmann (equation) models have been proposed [6–13]. The main feature of the LBE is to replace the particle occupation variables, n_i (Boolean variables) by the single-particle distribution functions (real variables) $f_i = \langle n_i \rangle$, where $\langle\ \rangle$ denotes a local ensemble average, in the evolution equation, i.e., the lattice Boltzmann equation.

The lattice Boltzmann equation as a numerical scheme was first proposed by McNamara and Zanetti [6]. In their model, the form of collision operator is the same as in the LGA, written in terms of distribution functions and completely neglecting the effects of correlations between the particles. Higuera, Jimenez, and Succi [7, 8] introduce a linearized collision operator that is a matrix and has no correspondence to the detailed collision rules. Statistical noise is completely eliminated in both models; however, the other problems remain, since the equilibrium distribution is still Fermi–Dirac. The lattice Boltzmann model proposed by Chen *et al.* [10, 12] and Qian *et al.* [9, 11] abandons Fermi–Dirac statistics and provides the freedom required for the equilibrium distribution to satisfy isotropy, Galilean invariance and to possess a velocity-independent pressure. The models in [10–12] apply the single relaxation time approximation first introduced by Bhatnager, Gross, and Krook in 1954 [14] to greatly simplify the collision operator. This model is called the lattice Boltzmann BGK model.

Compared with the lattice gas approach, the lattice Boltzmann method is more computationally efficient using current parallel computers. Applications have been done using both methods for hydrodynamics [15–18], flow through porous media [19, 20], magneto-hydrodynamics [21, 22], multiphase flow [23–26], and the reaction-diffusion equation [27–29]. Collected papers and applications of lattice gas and lattice Boltzmann methods can be found in [4, 5, 30–32].

Despite these studies on various problems, quantitative investigations of LGA and LBE are still scarce. There are some papers which include comparison of LBE with traditional computational methods [17, 18, 33]. In [17], a comparison between LBE and a finite difference method for the Navier–Stokes equations was done for the case of a double periodic jet flow. Kinetic energy as a function of time and vorticity contour at two times were compared for Re = 10,000. In [18], some global quantities as well as energy spectra were used for comparison between LBE and spectral method. In [33], LBE is only compared to a finite difference method of the Navier–Stokes equations for decaying Taylor vortex with Re = 100. The error averaged over some time period and over the whole field was used for the comparison. These comparisons indicate good agreement between LBE and traditional methods in most cases. However, all the aforementioned works used periodic flow without solid boundaries. Hence, it is important to do a thorough comparison in the presence of solid boundaries with complicated flow patterns over a wide range of Re numbers in order to give confidence to the engineering society about LBE. In the present work, the lattice Boltzmann BGK model (LBGK) is used to solve for the viscous flow in a square, two-dimensional cavity driven by shear due to one moving wall for Reynolds numbers up to 10,000. Detailed comparisons between the LBGK and traditional methods are presented. The compressibility error and the convergence rate of the method are discussed. The objective of this paper is to analyze the accuracy and physical fidelity of the lattice Boltzmann BGK method and to stimulate further studies using the lattice Boltzmann approach.

Section 2 presents a technical synopsis of the lattice Boltzmann model used in this paper that will enhance the general reader's understanding of this simulation method. More technical details are given in the Appendix for those who want to use the lattice Boltzmann method. The lattice Boltzmann simulation of driven cavity flow is discussed in Section 3 and thoroughly compared with results from other numerical methods. Section 4 studies the numerical errors in lattice Boltzmann simulations due to lattice size and compressibility. Section 5 is devoted to comparisons between the square lattice and the triangular (FHP) lattice. The limit of relaxation time for these two models is explored. The final section contains concluding remarks.

2. TWO-DIMENSIONAL SQUARE LATTICE BOLTZMANN MODEL

In this section an outline is given of the procedures of the lattice Boltzmann simulation. A square lattice with unit spacing is used on which each node has eight nearest neighbors connected by eight links (see Fig. A1 in the Appendix). Particles can only reside on the nodes and move to their nearest neighbors along these links in the unit time step. Hence, there are two types of moving particles. Particles of type 1 move along the axes with speed $|\mathbf{e}_{1i}| = 1$ and particles of type 2 move along the diagonal directions with speed $|\mathbf{e}_{2i}| = \sqrt{2}$. Rest particles with speed zero are also allowed at each node. The occupation of the three types of particles is represented by the single-particle distribution function, $f_{\sigma i}(\mathbf{x}, t)$, where subscripts σ and i indicate the type of particle and the velocity direction, respectively. When $\sigma = 0$, there is only f_{01}. The distribution function, $f_{\sigma i}(\mathbf{x}, t)$, is the probability of finding a particle at node $\mathbf{x}$ and time t with velocity $\mathbf{e}_{\sigma i}$. The particle distribution function satisfies the lattice Boltzmann equation

$$f_{\sigma i}(\mathbf{x} + \mathbf{e}_{\sigma i}, t + 1) - f_{\sigma i}(\mathbf{x}, t) = \Omega_{\sigma i}, \tag{1}$$

where $\Omega_{\sigma i}$ is the collision operator representing the rate of change of the particle distribution due to collisions. According to Bhatnagar, Gross, and Krook (BGK) [14], the collision operator is simplified using the single time relaxation approximation. Hence, the lattice Boltzmann BGK equation (in lattice units) is

$$f_{\sigma i}(\mathbf{x} + \mathbf{e}_{\sigma i}, t + 1) - f_{\sigma i}(\mathbf{x}, t) = -\frac{1}{\tau}[f_{\sigma i}(\mathbf{x}, t) - f^{(0)}_{\sigma i}(\mathbf{x}, t)], \quad (2)$$

where $f^{(0)}_{\sigma i}(\mathbf{x}, t)$ is the equilibrium distribution at $\mathbf{x}$, t, and τ is the single relaxation time which controls the rate of approach to equilibrium. The density per node, ρ, and the macroscopic velocity, $\mathbf{u}$, are defined in terms of the particle distribution function by

$$\sum_{\sigma}\sum_{i} f_{\sigma i} = \rho, \quad \sum_{\sigma}\sum_{i} f_{\sigma i}\mathbf{e}_{\sigma i} = \rho\mathbf{u}. \quad (3)$$

A suitable equilibrium distribution can be chosen in the following form for particles of each type [11]:

$$\begin{aligned} f^{(0)}_{0i} &= \tfrac{4}{9}\rho[1 - \tfrac{3}{2}u^2], \\ f^{(0)}_{1i} &= \tfrac{1}{9}\rho[1 + 3(\mathbf{e}_{1i}\cdot\mathbf{u}) + \tfrac{9}{2}(\mathbf{e}_{1i}\cdot\mathbf{u})^2 - \tfrac{3}{2}u^2], \\ f^{(0)}_{2i} &= \tfrac{1}{36}\rho[1 + 3(\mathbf{e}_{2i}\cdot\mathbf{u})^2 + \tfrac{9}{2}(\mathbf{e}_{2i} - \mathbf{u})^2 - \tfrac{3}{2}u^2]. \end{aligned} \quad (4)$$

The relaxation time is related to the viscosity by

$$\nu = \frac{2\tau - 1}{6}, \quad (5)$$

where ν is the kinematic viscosity measured in lattice units. A detailed derivation of the LBGK model is given in the Appendix.

Having chosen the appropriate lattice size and the characteristic velocity for the LBE system, the viscosity, ν, can be calculated for a given Re number and then the relaxation time can be determined by using (5). Starting from an initial density and velocity fields, the equilibrium distribution function can be obtained using Eq. (4), and $f_{\sigma i}(\mathbf{x}, t)$ can be initialized as $f^{(0)}_{\sigma i}(\mathbf{x}, t)$ (maybe with some corrections [44]). For each time step, the updating of the particle distribution can be split into two substeps: collision and streaming. It is irrelevant which one is the first for a long time run. The collision process at position $\mathbf{x}$ occurs according to the right-hand side of the lattice Boltzmann equation given as Eq. (2). The resulting particle distribution at $\mathbf{x}$, which is the sum of the original distribution and the collision term, is then streamed to the nearest neighbor of $\mathbf{x}$, $\mathbf{x} + \mathbf{e}_{\sigma i}$, for particle velocity $\mathbf{e}_{\sigma i}$. Then ρ, $\mathbf{v}$ can be computed from the updated $f_{\sigma i}(\mathbf{x}, t)$ using Eq. (3). The updating procedure can be terminated for steady state problems when certain criteria are reached. The method can also be used for transient problems.

The boundary condition commonly used at solid walls is the no-slip condition for which velocities vanish at the wall. This is implemented in the lattice gas and lattice Boltzmann methods with the bounce-back rule in which all particles hitting the wall are reflected back in the direction from which they came.

Another lattice model commonly used in two-dimensional lattice gas and lattice Boltzmann simulations is the triangular lattice (FHP model) [1, 2]. This is a two-speed (0 and 1) model in which the lattice constant (link) is equal to one. Simulations of cavity flow are also performed in this paper using this model. Comparisons between FHP and square lattice are discussed in Section 5. Two commonly used models for three-dimensional simulations are the 24-velocity FCHC [2] and the 14-velocity cubic models [11, 16].

3. CAVITY SIMULATION

The problem considered is two-dimensional viscous flow in a cavity. An incompressible fluid is bounded by a square enclosure and the flow is driven by a uniform translation of the top. The fluid motion generated in this cavity is an example of closed streamline problems that are of theoretical importance because they are part of a broader field of steady, separated flows. The literature is abundant for this flow configuration which shows rich vortex phenomena at many scales depending on the Reynolds number, Re. Numerical methods for solving the Navier–Stokes equations are often tested and evaluated on cavity flows because of the complexity of the flows.

Most numerical solutions of two-dimensional cavity flow [34–41] use a vorticity-stream function formulation and discretize the incompressible, steady linear or nonlinear Navier–Stokes equations by finite difference [34–37], multigrid [38, 40], and finite element [41] methods and their variations [39]. Earlier work was reviewed by O. Burggraf [34], where his numerical solutions of the nonlinear Navier–Stokes equations for Reynolds number up to 400 showed a large primary vortex and two secondary vortices in the lower corners. The later studies of Benjamin and Denny [37], Ghia, Ghia and Shin [38], Shreiber and Keller [39] show that tertiary vortices are formed near the bottom corners for higher Reynolds numbers. The present results using the lattice Boltzmann method are compared with those done by Vanka [40], Schreiber, and Keller [39], Ghia *et al.* [38]. Ghia *et al.* obtained numerical solutions up to Re = 10,000 with a 257 × 257 grid using the coupled strongly implicit multigrid method and the vorticity-stream function formulation. Their work is the most comprehensive study of cavity flow to date.

The present simulation uses Cartesian coordinates with the origin located at lower left corner. The top boundary moves from left to right with velocity U. The cavity has 256 lattice nodes on each side. Initially the velocities at all nodes, except the top nodes, are set to zero. The x-velocity of the top is U and the y-velocity is zero. Uniform fluid density $\rho = 2.7$ is imposed initially. Then the equilibrium particle distribution function, $f^{(0)}_{\sigma i}$, is calculated using Eq. (4), and $f_{\sigma i}$ is set to equal

to $f_{\sigma i}^{(0)}$ for all nodes at $t = 0$. The evolution of $f_{\sigma i}$ can then be found by a succession of streaming and relaxation processes. After streaming, the velocity of the top boundary is reset to its uniform initial velocity. At the end of each streaming and collision process cycle, $f_{\sigma i}$ at the top is set to the equilibrium state. Bounce-back boundary conditions are used on the three stationary walls. The two upper corners are singular points which are considered as part of the moving lid in the simulations, but tests shown there is little difference if these two points are treated as fixed wall points. The uniform velocity of the top wall used in the simulations is $U = 0.1$. Compressibility effects are discussed in Section 4.4. The Reynolds number used in the cavity simulation is $\mathrm{Re} = UL_N/\nu$, where U is the uniform velocity of the top plate, L_N is the number of lattice units along one side of the cavity, and ν is the kinematic viscosity as given in Eq. (5). All the results are normalized to allow comparisons between the present work and other results based on a unit square cavity with unit velocity of the top boundary.

Numerical simulations were carried out using the lattice Boltzmann method for Re = 100, 200, 400, 1000, 2000, 5000, 7500, and 10,000 on a 256 × 256 lattice (256 lattice nodes and 255 lattice units in one side). Steady-state solutions were obtained except for the last case because bifurcation takes place somewhere between Re = 7500 and 10,000. The results for Re = 10,000 oscillate between a series of different configurations. For this reason the results presented in this paper are those for Re up to 7500. The dependent variables of stream function, velocity, pressure, and vorticity are calculated using the particle distribution function, $f_{\sigma i}$. the dependent parameter of the drag coefficient of the driving wall is discussed also.

3.1. *Stream Function*

Figures 1a–f show plots of the stream function for the Reynolds numbers considered. It is apparent that the flow structure is in good agreement with the previous work of Benjamin and Denny [37], Schreiber and Keller [39], and Ghia *et al.* [38]. These plots give a clear picture of the overall flow pattern and the effect of the Reynolds number on the structure of the steady recirculating eddies in the cavity. In addition to the primary, center vortex, a pair of counterrotating eddies of much smaller strength develop in the lower corners of the cavity. At Re = 2000, a third secondary vortex is seen in the upper left corner. It is generated at a critical Re of about 1200, according to [37], in agreement with the results of the present work. For Re ≥ 5000, a tertiary vortex in the lower right-hand corner appears. A series of eddies with exponentially decreasing strength in the lower corners has been predicted by Ghia *et al.* [38].

For low Re (e.g., Re = 10), the center of the primary vortex is located at the midwidth and at about one-third of the cavity depth from the top. As Re increases (Re = 100), the primary vortex center moves towards the right and becomes increasing circular. Finally, this center moves down towards the geometric center of the cavity as the Re increases and becomes fixed in its x location for Re ≥ 5,000. the movement of the vortex center location versus Re is shown in Fig. 2 along with the results given by Ghia *et al.* [38].

To quantify these results, the maximum stream function value for the primary vortex and the minimum values for the secondary vortices along with the x and y coordinates of the center of these vortices are listed in Table I. All the results presented use a uniform top velocity $U = 0.1$, except for Re = 100, where $U = 0.01$ is used. The reason is discussed in Section 4.4. Also listed are results selected from previous work [38–40]. Previous results agree with each other for Re ≤ 1000, but they vary for higher values of Re. The results of the present work and that of Ghia *et al.* [38] for stream function values agree within 0.2% for all values of Re (Re = 2000 data was not given by [38]). The locations of the vortex centers predicted by the lattice Boltzmann method also agree well with those given by [38].

Unlike most finite-difference or finite-element methods that start from the steady-state, partial differential equations, the present method is an unsteady approach in which the solution evolves into steady state. The time to reach steady state depends on the lattice size, the values of Re, the driving velocity, U, and the initial condition. For all the cases run in this paper, steady state is reached when the difference between the maximum values of the stream function for successive 10,000 steps (process cycles) is less than 10^{-5}. Considering the kinetic, compressible, and unsteady nature of the lattice Boltzmann method, the excellent agreement with entirely different methods such as Ghia *et al.* [38] is quite encouraging.

The minimum values of stream function and the center of the secondary vortex in the upper left corner for Re = 5000 and 7500 are listed in Table II. These results also show good agreement with Ghia *et al.* [38].

3.2. *Velocity Profiles*

Velocity components along a vertical and horizontal center lines for several values of Re are shown in Fig. 3. the velocity profiles change from curved at lower values of Re to linear for higher Re values. The near linear profiles of the velocity in the central core of the cavity indicate the uniform vorticity region generated in the cavity at higher values of Re. These results agree with those from previous studies [36, 38, 39].

3.3. *Vorticity*

The plots of vorticity in Figs. 4a–f show that the steady cavity flow within closed streamlines at high Re consists of a central, inviscid core of nearly constant vorticity with viscous effects confined to thin shear layers near the walls. Batchelor [42] predicted these results from his model for separated eddies in a steady flow. As Re increases, several regions of high vorticity gradients (indicated by concentration of the vorticity contours) appear within the cavity. The thinning of the wall boundary layers with increasing Re is evident from these plots,

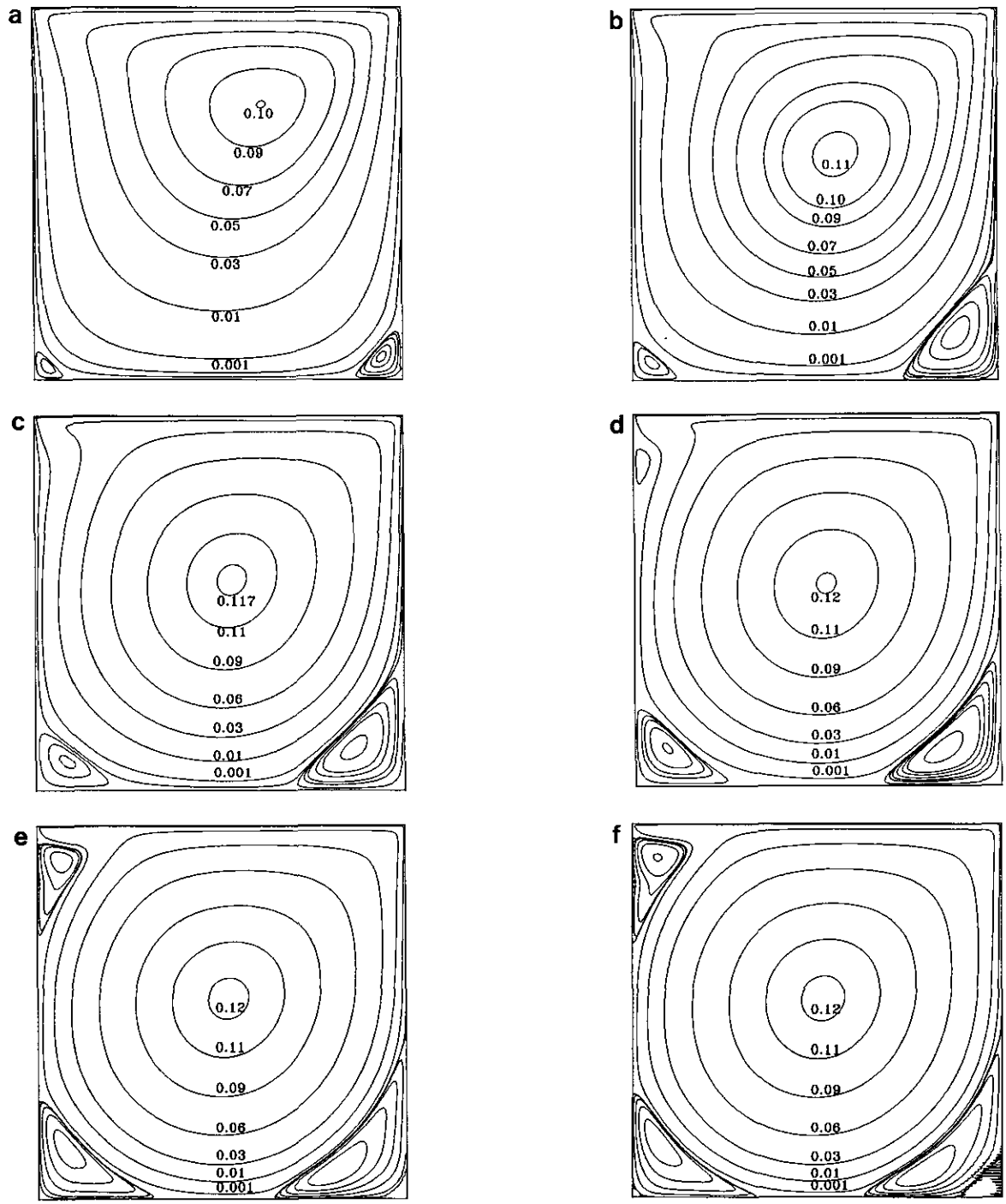

FIG. 1. (a) Stream function for Re = 100. Top velocity $U = 0.01$. The center of the primary vortex is at (0.6196, 0.7373). The center of lower left vortex is at (0.0392, 0.0353). The center of lower right vortex is at (0.9451, 0.0627). (b) Stream function for Re = 400. Top velocity $U = 0.1$. The center of the primary vortex is at (0.5608, 0.6078). The center of lower left vortex is at (0.0549, 0.0510). The center of lower right vortex is at (0.8902, 0.1255). (c) Stream function for Re = 1000. Top velocity $U = 0.1$. The center of the primary vortex is at (0.5333, 0.5647). The center of lower left vortex is at (0.0902, 0.0784). The center of lower right vortex is at (0.8667, 0.1137). (d) Stream function for Re = 2000. Top velocity $U = 0.1$. The center of the primary vortex is at (0.5255, 0.5490). The center of lower left vortex is at (0.0902, 0.1059). The center of lower right vortex is at (0.8471, 0.0980). (e) Stream function for Re = 5000. Top velocity $U = 0.1$. The center of the primary vortex is at (0.5176, 0.5373). The center of lower left vortex is at (0.0784, 0.1373). The center of lower right vortex is at (0.8078, 0.0745). (f) Stream function for Re = 7500. Top velocity $U = 0.1$. The center of the primary vortex is at (0.5176, 0.5333). The center of lower left vortex is at (0.0706, 0.1529). The center of lower right vortex is at (0.7922, 0.0667).

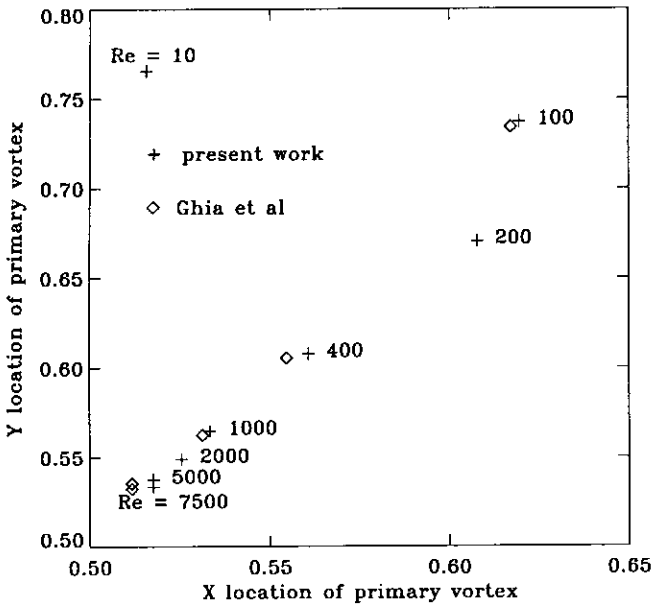

FIG. 2. The locations of the center of the primary vortex for different values of Re numbers. The origin is the geometric center of the cavity.

although the rate of this thinning is very slow for Re $\geq$5000. The values of vorticity at the center of the primary vortex for different Re are listed in Table III. These values closely agree with the results of Ghia *et al.* [38] and approach the analytical value of 1.886 for an infinite Reynolds number calculated by Burggraf [34] using Batchelor's model.

3.4. *Pressure*

Figures 5a–f displays the pressure deviation contours for the present simulations. Since only the pressure gradient appears in the Navier–Stokes equation, the pressure values can differ by a constant. These plots are in good agreement with the static pressure given by Burggraf [34]. Note that the top wall in [34] moves from right to left which is opposite to that in the present simulation. The pressure in [34] is obtained by integrating the Navier–Stokes equation given the velocity field, while the pressure in the lattice Boltzmann method satisfies the equation of state of an isothermal gas given by $p = c_s^2 \rho$ (see the Appendix). The observed agreement between these very different approaches demonstrates that the lattice Boltzmann BGK model is valid for simulating incompressible flow. By examining the closed contours in the pressure plots, it is seen that the inviscid core grows with increasing values of Re. The pressure contours (and streamlines) presented in this paper are exactly the same as those in [43] by J. L. Sohn for all of the values of Re studied.

TABLE I

Vortex Centers: Stream Function and Location

		Primary vortex			Lower left vortex			Lower right vortex		
Re		ψ_{max}	x	y	ψ_{min}	x	y	ψ_{min}	x	y
100	a	0.1034	0.6188	0.7375	−1.94e-6	0.0375	0.0313	−1.14e-5	0.9375	0.0563
	b	0.1034	0.6172	0.7344	−1.75e-6	0.0313	0.0391	−1.25e-5	0.9453	0.0625
	c	0.1033	0.6167	0.7417	−2.05e-6	0.0333	0.0250	−1.32e-5	0.9417	0.0500
	d	0.1030	0.6196	0.7373	−1.72e-6	0.0392	0.0353	−1.22e-5	0.9451	0.0627
400	a	0.1136	0.5563	0.6000	−1.46e-5	0.0500	0.0500	−6.45e-4	0.8875	0.1188
	b	0.1139	0.5547	0.6055	−1.42e-5	0.0508	0.0469	−6.42e-4	0.8906	0.1250
	c	0.1130	0.5571	0.6071	−1.45e-5	0.0500	0.0429	−6.44e-4	0.8857	0.1143
	d	0.1121	0.5608	0.6078	−1.30e-5	0.0549	0.0510	−6.19e-4	0.8902	0.1255
1000	a	0.1173	0.5438	0.5625	−2.24e-4	0.0750	0.0813	−1.74e-3	0.8625	0.1063
	b	0.1179	0.5313	0.5625	−2.31e-4	0.0859	0.0781	−1.75e-3	0.8594	0.1094
	c	0.1160	0.5286	0.5643	−2.17e-4	0.0857	0.0714	−1.70e-3	0.8643	0.1071
	d	0.1178	0.5333	0.5647	−2.22e-4	0.0902	0.0784	−1.69e-3	0.8667	0.1137
2000	a	0.1116	0.5250	0.5500	−6.90e-4	0.0875	0.1063	−2.60e-3	0.8375	0.0938
	d	0.1204	0.5255	0.5490	−7.26e-4	0.0902	0.1059	−2.44e-3	0.8471	0.0980
5000	a	0.0921	0.5125	0.5313	−1.67e-3	0.0625	0.1563	−5.49e-3	0.8500	0.0813
	b	0.1190	0.5117	0.5352	−1.36e-3	0.0703	0.1367	−3.08e-3	0.8086	0.0742
	d	0.1214	0.5176	0.5373	−1.35e-3	0.0784	0.1373	−3.03e-3	0.8078	0.0745
7500	b	0.1200	0.5117	0.5322	−1.47e-3	0.0645	0.1504	−3.28e-3	0.7813	0.0625
	d	0.1217	0.5176	0.5333	−1.51e-3	0.0706	0.1529	−3.20e-3	0.7922	0.0667

Note: a, S. P. Vanka [40]; b, U. Ghia, K. N. Ghia, and C. T. Shin [38]; c, R. Schreiber and H. B. Keller [39]; d, present work.

TABLE II

Upper Left Vortex: Stream Function and Location

Re		Upper left vortex		
		ψ_{min}	x	y
5000	a	−1.46e-3	0.0625	0.9102
	b	−1.40e-3	0.0667	0.9059
7500	a	−2.05e-3	0.0664	0.9141
	b	−2.06e-3	0.0706	0.9098

Note. a, U. Ghia, K. N. Ghia, and C. T. Shin [38]; b, present work.

3.5. *Drag on the Top*

The drag force and the drag coefficient of the moving wall are calculated here for Re values considered in the study. The stress on the moving wall is given by the Newton's formula:

$$\tau_{yx} = \mu \frac{\partial u}{\partial y},$$

where u is the x component of velocity and μ is the kinetic viscosity. The drag force on this surface, F_d, is defined and computed as

$$F_d = \int_0^L \tau_{yx} dx = \int_0^L \mu \frac{\partial u}{\partial y} dx \approx \mu \sum_{i=1}^{n_x - 1} \frac{u(i, ny) - u(i, ny-1)}{\Delta y} \Delta x,$$

where n_x is the grid number in the x direction, L is the length of the square cavity, and $\Delta y = \Delta x = L/(n_x - 1)$ are the lattice spacing. The drag coefficient is then written as

$$C_d = \frac{F_d}{\bar{\rho} U^2 L},$$

where $\bar{\rho}$ is the average density and U is the velocity of the top. The drag coefficient decreases as Re increases, as found in other laminar flow configurations. This can be seen by introducing the dimensionless quantities

$$u' = \frac{u}{U}, \quad x' = \frac{x}{L}, \quad y' = \frac{y}{L}.$$

The drag coefficient can then be expressed as

$$C_d = \frac{U \int_0^1 \mu(\partial u'/\partial y')\, dx'}{\bar{\rho} U^2 L} = \int_0^1 \frac{\mu}{\bar{\rho} U L} \frac{\partial u'}{\partial y'} dx' = \frac{1}{\mathrm{Re}} \int_0^1 \frac{\partial u'}{\partial y'} dx'.$$

The results of drag and drag coefficients for different values of Re are listed in Table IV and the drag coefficient is plotted as a function of Re in Fig. 6.

4. ERROR ANALYSIS

4.1. *Sources of Errors*

There is no analytic solution for cavity flow. Results from the work described in this paper are compared with the numerical

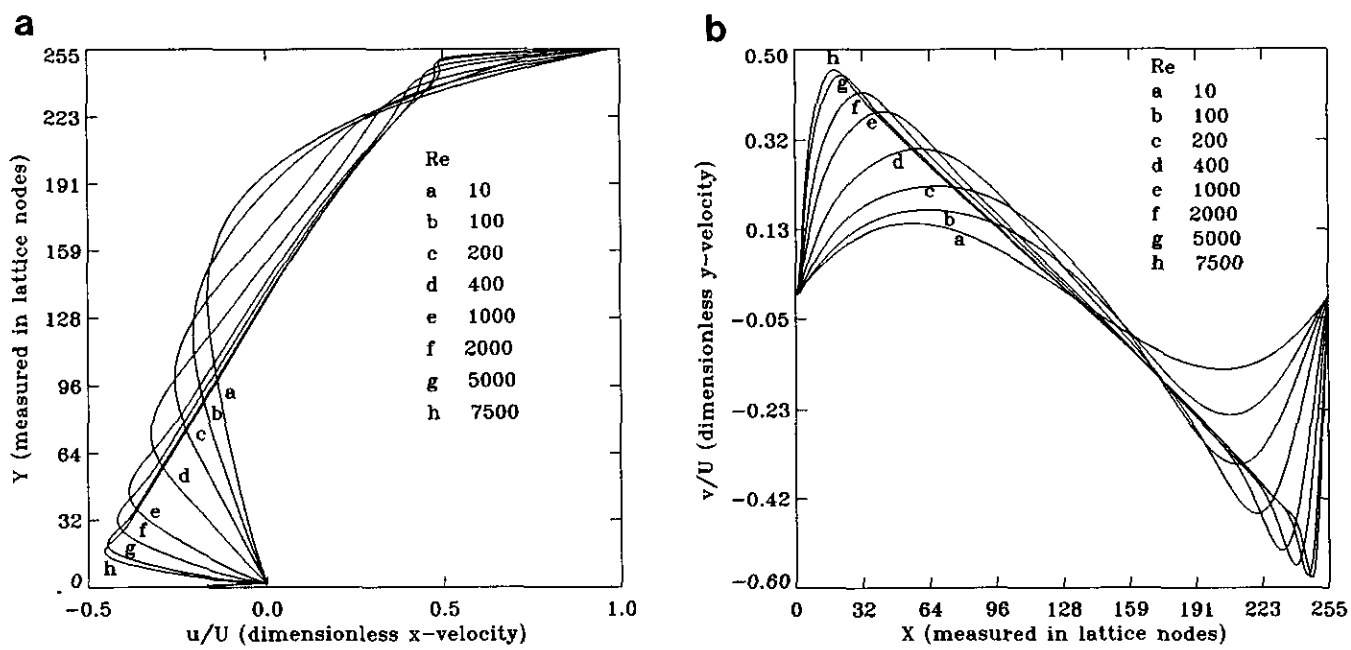

FIG. 3. (a) Velocity profiles for u through the geometric center of the cavity. (b) Velocity profiles for v through the geometric center of the cavity.

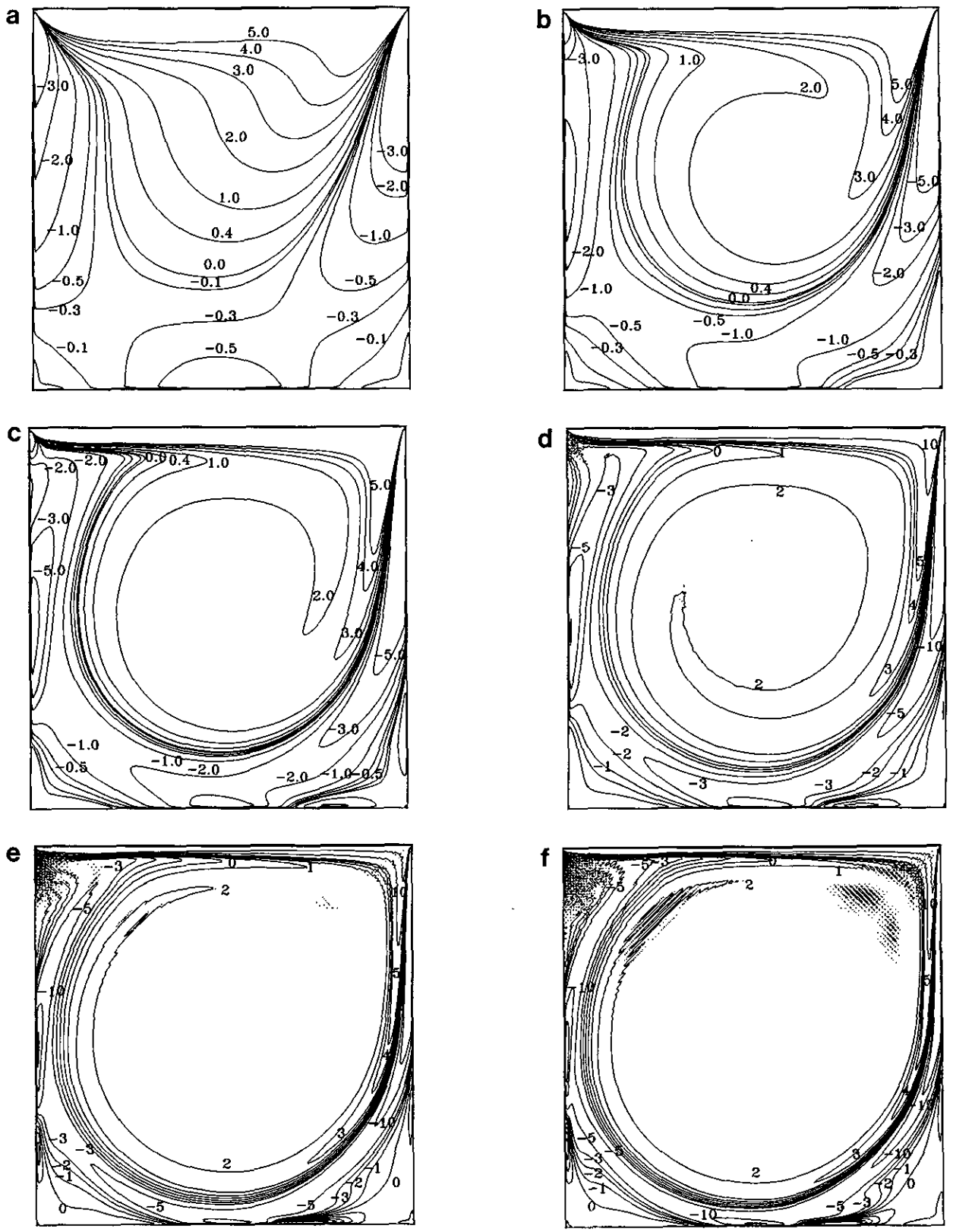

FIG. 4. Vorticity contours of the cavity flow: (a) Re = 100; (b) Re = 400; (c) Re = 1000; (d) Re = 2000; (e) Re = 5000; (f) Re = 7500.

TABLE III

Vorticity in the Center of Primary Vortex

	Reynolds number				
$\Omega_{v,c}$	100	400	1,000	5,000	7,500
a	3.1665	2.2947	2.0497	1.8602	1.8799
b	3.1348	2.2910	2.0760	1.9384	1.9014

Note. a, U. Ghia, K. N. Ghia, and C. T. Shin [38]; b, present work.

solutions obtained by several other methods. Differences are found between the results of previous calculations, especially for higher values of Re. Several of these authors state that the data for the secondary vortices are less reliable due to corner singularities and/or roundoff errors [39], mesh-size limitations [36], or because the values of the stream function in the corners are small and, in some cases, below the convergence accuracy of the calculations [40].

Our early results from lattice Boltzmann simulations were very close to the results given by Ghia *et al.* [38] for Re $\geq$ 1000. However, the properties of the secondary vortices were less satisfactory for Re $<$ 1000. The secondary vortex of the lower left corner for Re = 100, whose stream function is a small quantity of the order of 10^{-6}, was not detected. Also, the secondary vortex in the lower right corner for the same Re, whose stream function is of the order of 10^{-5}, did not match corresponding results of other investigators. Although these are not major features, it was important to investigate the cause of these discrepancies and to make improvements.

The theoretical assumptions of the present method are the Boltzmann transport equation, plus the single relaxation time approximation of the collision term. As long as the macroscopic properties of fluid vary slowly enough in space and time, compared with microscopic particle dynamics, collisions should maintain approximately the local equilibrium such that the assumptions of molecular chaos by Boltzmann and single relaxation time by BGK are valid for problems of fluid dynamics. The possible reasons for the "errors" in the present simulations may be categorized as follows:

1. The simulations done for different values of Re on a 256 $\times$ 256 lattice used single precision arithmetic in CM200 due to limited computer sources. It is possible that roundoff error could be accumulated.

2. The small compressibility effect presented in the LBE simulations may cause differences when compared with models where compressibility is zero.

3. The lattice used here may still be too coarse to resolve all the small scale phenomena.

4. The time step at which the simulation is terminated may not be large enough to represent the steady state.

5. The integration methods used in the calculation of the stream function may introduce errors.

To check errors caused by 1 and 4, experiments using double precision floating-point arithmetic and running for longer times were carried out. These experiments did not change the main results nor improve on finding weak vortices on the smaller scales, indicating that errors due to 1 and 4 are small compared with other errors. What follows are subsections investigating the remaining error sources.

4.2. *Effect of Lattice Size*

To test the effect of lattice size, simulations for Re = 1000 were done on the following lattice configurations: 33 $\times$ 33, 65 $\times$ 65, 129 $\times$ 129, 257 $\times$ 257, and 513 $\times$ 513. The driving velocity used was fixed at $U = 0.1$. Two relative velocity errors, the $L1$ and $L2$ errors, were calculated according to the following formula:

$$E1 = \frac{\sum_{x,y} |u_1 - u_0| + |v_1 - v_0|}{\sum_{x,y} |u_0| + |v_0|},$$

$$E2 = \frac{\sqrt{\sum_{x,y} (u_1 - u_0)^2 + (v_1 - v_0)^2}}{\sqrt{\sum_{x,y} (u_0)^2 + (v_0)^2}},$$

where u, v are the x and y components of the velocity, respectively. The subscripts 0, 1 indicate the 513 $\times$ 513 and the coarser grain lattice, respectively. Velocities on different grids are taken at corresponding positions, while the sums are taken over the entire lattice.

The results for $E1$ and $E2$ are plotted logarithmically in Fig. 7 and listed in Table V. It is clear from Fig. 7 that the convergence rate is approximately first order in space. This result is different from other works [17, 44], where a second-order convergence rate is claimed. In [17] a decaying Taylor vortex flow with periodic boundary conditions (no solid walls) is treated and in [44] more complicated and accurate boundary conditions for the particle distribution function are used instead of the bounce-back condition implemented at the wall in the present work. The first order convergence rate observed here may be due to the bounce-back condition used on the stationary walls. This observation is confirmed by a recent paper [45] in which the bounce-back boundary condition is shown to be a first-order approximation to a no-slip wall.

Better resolution is obtained as the number of lattice nodes increases. However, computer time grows with the lattice number because more nodes are updated and the time to reach steady state increases. Of course, the number of time steps required to reach steady state strongly depends on initial conditions. Table VI gives an idea how the number of time steps varies with the lattice size for fixed initial conditions. A simulation run on a 513 $\times$ 513 lattice for Re = 100 did not improve the method's ability to predict the secondary vortex in the lower left corner.

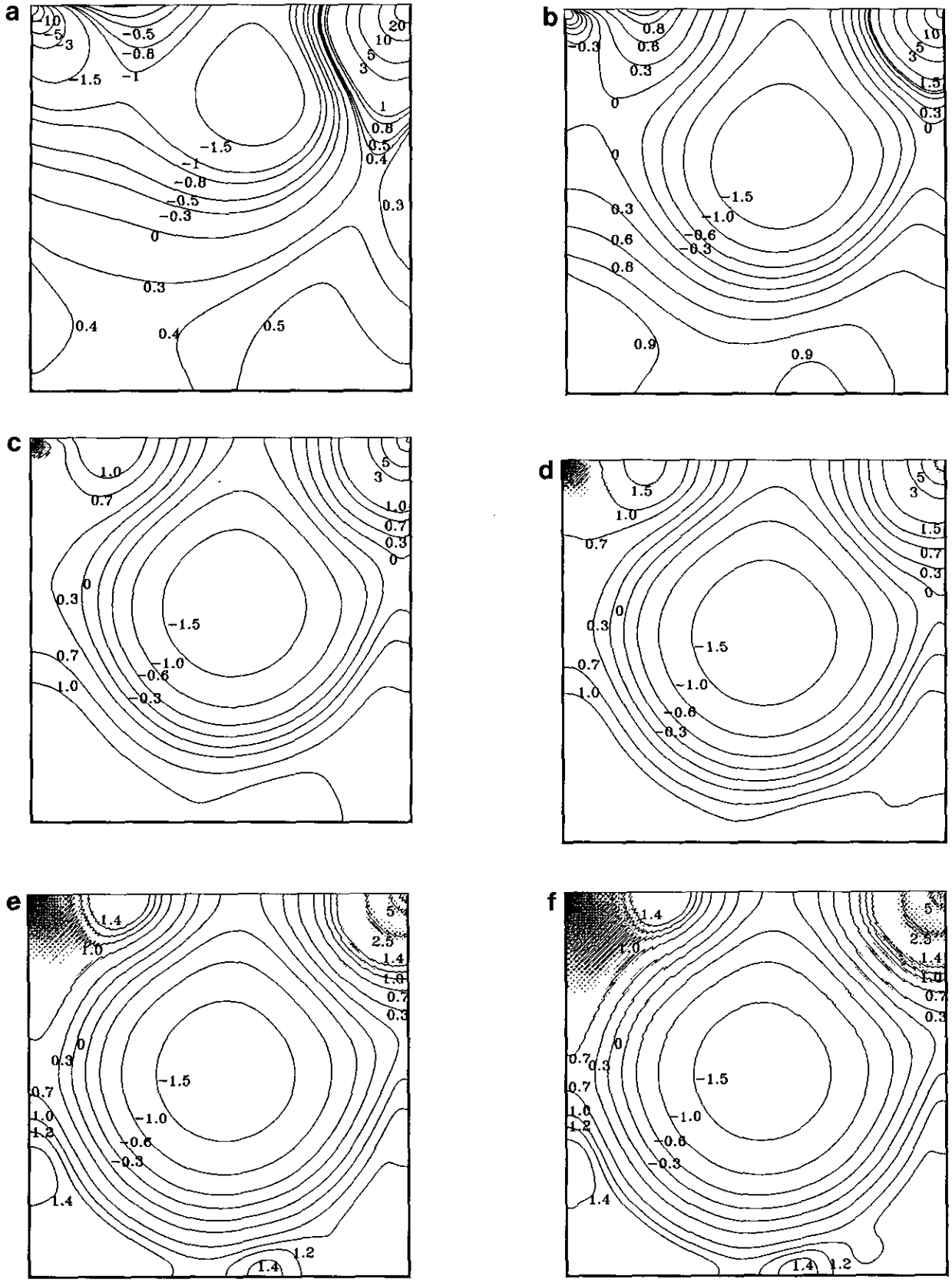

FIG. 5. Pressure deviation contours of the cavity flow (the value has been multiplied by 1000): (a) Re = 100; (b) Re = 400; (c) Re = 1000; (d) Re = 2000; (e) Re = 5000; (f) Re = 7500.

TABLE IV

Drag and Drag Coefficient of the Top

Re	100	200	400	1000	2000	5000	7500
F_d	1.45	0.59	0.28	0.14	0.08	0.05	0.03
C_d	56.90	23.27	10.86	5.31	3.12	1.67	1.28

4.3. *Integration Error*

The most important features of the cavity flow are described by the stream function. The stream function used by Ghia *et al.* [37] (and others) was the primary variable. In the lattice Boltzmann model, however, the primary variable is the particle distribution function, $f_{\sigma i}$. The velocity at each site is calculated from $f_{\sigma i}$ and the stream function is obtained by integrating the velocities.

To investigate the error caused by integration, three integration rules (rectangular, trapezoidal, and Simpson) were used for Re = 100. The results from all three rules are quite close if the integrations are taken in the same direction. Significantly different results are obtained by integrating from the four different directions, namely integrating u along y from top to bottom or from bottom to top and integrating v along x from left to right or from right to left. Theoretically, they should all give the same value for the stream function.

From a numerical point of view, the integration should be taken from the smaller scale; otherwise the smaller scale would be drowned into roundoff error. However, in this particular case, integration from bottom to top contains significant error.

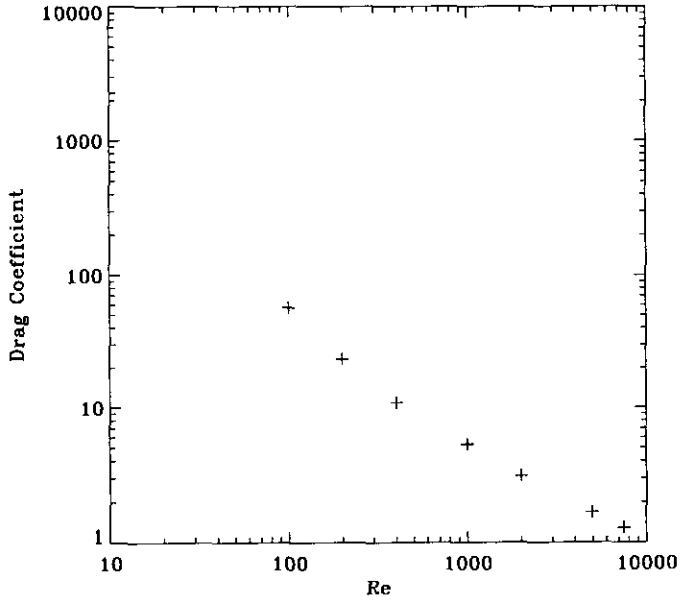

FIG. 6. Drag coefficient of top wall versus Re.

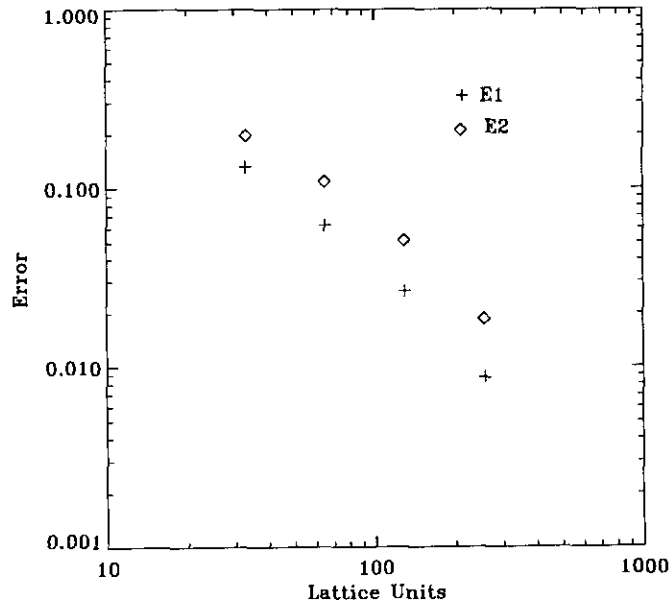

FIG. 7. Convergence rate of the LBE method for Re = 1000 with top velocity $U = 0.1$. The errors are calculated relative to results obtained on a 513 × 513 lattice.

The reason can be seen from the error formula. If the trapezoidal rules is used,

$$I(f) = \int_a^b f(x)\,dx$$

$$\approx h\left[\frac{1}{2}f(a) + f(a+h) + \cdots + \frac{1}{2}f(b)\right] = I_n(f),$$

where $h = (b - a)/n$ and n is the number of subdivisions within $\{a, b\}$, the integration error can be approximated by the asymptotic error formula [43]:

$$E_n(f) \approx -\frac{h^2}{12}[f'(b) - f'(a)].$$

The factor, $h^2/12$, in the present case is about 1.3×10^{-6}. The

TABLE V

Relative Velocity Error Caused by Lattice Size

Lattice size	33 × 33	65 × 65	129 × 129	257 × 257
E_1	0.1316	0.0623	0.0264	0.0087
E_2	0.1968	0.1088	0.0512	0.0185

Note. Re = 1000; E_1 and E_2 are based on 513 × 513 lattice.

TABLE VI

Time Steps to Reach Steady State for Different Lattice Sizes

Lattice size	33 × 33	65 × 65	129 × 129	257 × 257	513 × 513
Time steps	60,000	100,000	200,000	350,000	600,000

Note. Re = 1000.

error then depends on the derivatives at the end points. In the case of integration taken from top to bottom or from bottom to top, the two derivatives have opposite signs and the error is enhanced. In addition, the value of the derivative at the top is large. On the other hand, integration from left to right or from the right to left has the same signs on the two end derivatives, therefore decreasing the integration error. Since the left corner vortex is smaller than the right, the integration taken from left to right gives better results than the integration taken from the right to the left. Therefore, the trapezoidal rule is used to integrate v from left to right to calculate the stream function. The error is then of order of 10^{-9} according to the asymptotic error formula.

4.4. *Compressibility Effect*

It has been shown that the present LBE model represents the Navier–Stokes equation in the incompressible limit (see the Appendix). But in the LBE simulation, the density cannot be a constant (otherwise pressure changes cannot be described). It is important to find the effect of compressibility on the present solution.

One quantity that represents compressibility is the mean variation of density. The mean density is defined as

$$\bar{\rho} = \frac{\sum_i \rho(x_i, t)}{N},$$

where N is the total number of nodes. The mean variation of density is given by

$$\Delta = \frac{1}{\bar{\rho}} \sqrt{\sum ((\rho - \bar{\rho})^2)/N}.$$

For Re = 100, this mean density fluctuation, Δ, is calculated for $U = 0.1$, $U = 0.05$, $U = 0.01$ and listed in Table VII,

TABLE VII

Mean Density Fluctuation

U	0.1	0.05	0.01
M	0.173	0.0867	0.0173
Δ	2.6×10^{-3}	7.4×10^{-4}	5.6×10^{-5}

Note. Re = 100.

along with the Mach number, $M = u/c_s$, where $c_s = 1/\sqrt{3}$ is the speed of sound for the present model. The table shows that

$$\Delta(U = 0.05) \approx \tfrac{1}{4}\Delta\ (U = 0.1)$$

and

$$\Delta(U = 0.01) \approx \tfrac{1}{25}\Delta\ (U = 0.05)$$

These results agree with the known relationship [18] that Δ is proportional to M^2. (This relation can be seen from the dimensionless incompressible Navier–Stokes equations.)

The compressibility effect can also be examined for the cavity flow problem as follows. In the steady case, the continuity equation represented by the LBE is $\nabla \cdot (\rho \mathbf{u}) = 0$. Due to a non-constant ρ, the velocity $\mathbf{u}$ does not satisfy the incompressible continuity equation given by $\nabla \cdot \mathbf{u} = 0$ exactly. It is from this equation that the stream function can be defined using $u = \partial\psi/\partial y$ and $v = -\partial\psi/\partial x$, where ψ is the stream function. There is actually no exact definition for the stream function in the LBE. Given a discrete velocity field obtained from the LBE calculation, an approximation of the stream function for the incompressible flow with $\nabla \cdot \mathbf{u} = 0$ needs to be constructed. The stream function definition written as $\psi = \int -v\,dx + u\,dy$ is still used to calculate the stream function. When integrating in only the x- or y-direction, the integral becomes $\psi = \int_0^y u\,dy$, or $\psi = -\int_0^x v\,dx$. In the case of incompressible flow in a cavity, the boundaries coincide with the zero stream function. The integrals then take the form

$$\psi = \int_0^L u\,dy = \int_0^L v\,dx = 0,$$

where L is the total length of the wall. In the actual computations, however, the stream function at the end wall will not exactly equal zero because of roundoff and integration errors. Due to the additional effects of compressibility in the LBE method, if the stream function is calculated by integrating v from the left to the right edge of the cavity, the values of the stream function on the right wall would indicate the error caused by compressibility, roundoff, and integration errors. Since the trapezoidal rule gives the same results for integrations taken from opposite directions if there is no roundoff error, the roundoff error is found by comparing the values of the stream function on the left and right walls taken from opposite directions (the other sources of error, compressibility and integration, are the same for these two integrals). This error is less than about 10^{-9}. The integration error is of the order of 10^{-9} as discussed above. Therefore, the maximum and the mean value of ψ at the right wall can be computed as an indicator of error due to compressibility if this value is larger than 10^{-8}. The mean and maximum stream function at the right edge of the cavity is defined, respectively, as

TABLE VIII

Compressibility Effect

U	0.1	0.05	0.01
M	0.173	0.0867	0.0173
S_a	2.4×10^{-4}	6.4×10^{-5}	2.7×10^{-6}
S_m	6.7×10^{-4}	1.8×10^{-4}	8.1×10^{-6}

Note. Re = 100.

$$S_a = \sqrt{\sum_j (\psi^2(n_x, j))/n_y}$$

and

$$S_m = \max_j |\psi(n_x, j)|,$$

where $n_x = n_y = 256$ is the number of nodes in the x- and y-directions, respectively. These values are calculated for $U = 0.1$, $U = 0.05$, and $U = 0.01$ for Re = 100 and listed in Table VIII. Again, the results show that S_a and S_m are proportional to M^2. These values can be used as a quantitative measure of the compressibility error of the LBE method. The change of compressibility error with Re is calculated for $U = 0.1$ and listed in Table IX. The compressibility error does not vary much with Re. With increasing Re, the error decreases slightly, but it is still of the same order of magnitude.

The compressibility error measured by S_a and S_m has about the same order effect as the small scale phenomena in the cavity flow for low values of Re. Nevertheless, by choosing an appropriate direction of integration for the stream function, predictions of the small vortices are still obtained as given in Table I. Furthermore, the compressibility error can be reduced by using smaller velocities at the top boundary. The results for Re = 100 in Table I are calculated using $U = 0.01$, while other Reynolds number use $U = 0.1$. However, the time steps required to reach steady state for smaller top velocities increases dramatically. To overcome the compressibility error in the present LBE model, a new incompressible LBE model for steady-state flow has been developed and will be published in another paper [47].

5. TRIANGULAR LATTICE (FHP) VERSUS SQUARE LATTICE

Simulations for cavity flow are also carried out on a triangular lattice (FHP). There are two types of particles on each node of an FHP model: rest particles and moving particles with unit velocity $\mathbf{e}_i$ along six directions. In analogy to the procedures used for the square lattice in the Appendix, the equilibrium distributions for the FHP model are given as

$$f_0^{(0)} = d_0 - \rho u^2 = \alpha\rho - \rho u^2,$$

$$f_i^{(0)} = d + \tfrac{1}{3}\rho[(\mathbf{e}_i \cdot \mathbf{u}) + 2(\mathbf{e}_i \cdot \mathbf{u})^2 - \tfrac{1}{2}u^2]$$

$$= \frac{\rho - \alpha\rho}{6} + \tfrac{1}{3}\rho[(\mathbf{e}_i \cdot \mathbf{u}) + 2(\mathbf{e}_i \cdot \mathbf{u})^2 - \tfrac{1}{2}u^2],$$

where α is an adjustable parameter. If the ratio of rest and moving particles is defined as $\lambda = d_0/d$, the pressure is determined by the isothermal equation of state,

$$p = 3d = \frac{(1-\alpha)\rho}{2} = \frac{3}{\lambda + 6}\rho,$$

and the speed of sound is

$$c_s^2 = \frac{1-\alpha}{2} = \frac{3}{\lambda + 6}.$$

The viscosity is related to the relaxation time through an equation of the form

$$\nu = \frac{2\tau - 1}{8}.$$

Theoretically, the relaxation time, τ, cannot be lower than 0.5 for a positive viscosity. To reach higher Re, the relaxation time can be lowed. Tests on a 128×128 lattice with a maximum velocity of $U = 0.1$ show that a critical value for τ exists. Above this value, the simulation is smooth and reasonable physical patterns for the cavity flow are seen in the real-time plots. However, below this critical value, some nonphysical patterns appear. Further reduction in the value of τ would cause

TABLE IX

Compressibility Effect with Re

Re	100	200	400	1000	2000	5000	7500
S_a	2.4×10^{-4}	1.5×10^{-4}	1.0×10^{-4}	6.4×10^{-5}	4.8×10^{-5}	3.8×10^{-5}	3.8×10^{-5}
S_m	6.7×10^{-4}	4.6×10^{-4}	3.2×10^{-4}	2.1×10^{-4}	1.5×10^{-4}	1.1×10^{-4}	8.7×10^{-4}

Note. $U = 0.1$.

TABLE X

Lowest Relaxation Time for FHP Model, $U = 0.1$, Case 1

λ	1	2	3	4	5	6	8	10
c_s	0.655	0.612	0.577	0.548	0.522	0.500	0.463	0.433
M	0.153	0.163	0.173	0.182	0.192	0.200	0.215	0.231
τ_{min}	0.533	0.528	0.527	0.526	0.525	0.520	0.518	0.516
Re_{max}	1551	1829	1896	1969	2048	2560	2844	3200

Note. $U = 0.1$, 128×128 lattice.

TABLE XII

Lowest Relaxation Time for FHP Model, $U = 0.01$, Case 2

λ	1	2	6
c_s	0.655	0.612	0.500
M	0.015	0.016	0.0200
τ_{min}	0.560	0.520	0.519
Re_{max}	85.3	256	269.5

Note. $U = 0.01$, 128×128 lattice.

the simulation to be terminated by numerical blowup. Define the critical value of τ as the lowest limit for the relaxation time that gives physically correct results. This limit varies with the ratio, λ, maximum velocity, U, and the problem studied. If λ is increased, the speed of the sound will be decreased and the Mach number is then increased if the velocity is unchanged. Table X lists the lowest relaxation time, τ_{min}, and hence the highest Re number, Re_{max}, obtained for different λ, along with their speed of sound, c_s, and Mach number, M. Table X shows that the highest Re can be increased by increasing λ. However, the compressibility error is also increased.

Table XI lists results for the same conditions as in Table X, but for slightly different initial boundary conditions on $f_{\sigma i}$. In Table X (case 1), the initial fluid density on each node of the stationary walls is the same as that for interior nodes. In Tables XI–XII the initial density on the stationary walls is set equal to zero. It is clear that when $\lambda = 1$, the lowest τ is much higher than that in Table X, but for large λ the differences of τ_{min} between these two cases are diminished. The rest particles in the LBE method play the role of a particle reservoir. When the macroscopic velocity is higher, rest particles can be turned into moving particle and *vice versa*. Higher values of $\lambda = d_0/d$ mean that a larger fraction of rest particles in the density behave like a fluid that is less rigid and more flexible (the compressibility is higher). When $\lambda = 1$ in case 2, the lowest value of τ for stable results is 0.5668. However, setting $\tau = 0.5667$ would make the computation blow up immediately due to the large initial density gradient on the wall and the relatively small fraction of rest particles. The lowest limit of τ does not depend on the lattice size. Changing the maximum velocity, U, does change the lowest τ slightly. However, the highest Re numbers obtainable by this approach are much lower than that for $U = 0.1$ (see Table XII for case 2).

TABLE XI

Lowest Relaxation Time for FHP Model, $U = 0.1$, Case 2

λ	1	2	3	4	5	6	8	10
c_s	0.655	0.612	0.577	0.548	0.522	0.500	0.463	0.433
M	0.153	0.163	0.173	0.182	0.192	0.200	0.215	0.231
τ_{min}	0.567	0.529	0.526	0.524	0.523	0.523	0.520	0.520
Re_{max}	764	1766	1969	2133	2226	2226	2560	2560

Note. $U = 0.1$, 128×128 lattice.

The square lattice corresponds to $\lambda = d_0/d_1 = 4$. Tests on a 128×128 square lattice with the maximum velocity of $U = 0.1$ show that the value of τ cannot be smaller than 0.507 (Re = 5485) for cavity flow. Hence, a simulation run on a 256×256 lattice with $U = 0.1$ can reach Re = 10,000 ($\tau = 0.50768$) which is about the highest limit of Re on this size lattice for cavity flow. Using small U did not produce a further reduction of τ. The square lattice is better than the FHP lattice in the cavity flow simulations because the former can reach higher values of Re than the latter for the same maximum velocity and lattice size. Since the boundaries of the cavity are fitted better using the square lattice than the FHP lattice, the formation of the vortices is more gentle in the simulation using a square lattice than an FHP lattice. The ranges of parameters presented in this section are consistent with the results of linear stability analysis of the LBE method without boundaries [48].

6. CONCLUSIONS

The lattice Boltzmann method is a derivative of the lattice gas automata method and therefore inherits from the LGA some of its advantages over traditional computational methods. It is parallel in nature due to the locality of particle interaction and the transport of particle information, so it is well suited to massively parallel computing. The lattice Boltzmann method easily handles complex boundary conditions and complex properties of a fluid system, such as flow through porous media and multi-phase flow. One important improvement due to the LBE method is that it can fully recover the exact Navier–Stokes equations at the macroscopic level. However, there is a trade-off. The lattice Boltzmann method is no longer purely Boolean and it does not have the robust numerical stability guaranteed in the LGA.

Detailed studies of the cavity flow problem using the lattice Boltzmann method has shown that the method is accurate, compared with conventional methods using the same mesh size. This verification gives one confidence to apply the method to other complex systems. All aspects of the present work such as boundary conditions, parameter ranges, lattice size, and com-

pressibility effects are important when the method is applied to other problems. The following remarks are in order:

1. The proper implementation of the boundary conditions is crucial for the lattice Boltzmann simulation. Various boundary conditions such as periodic, particle bounce-back, wind tunnel, and constant flux conditions are commonly used for different situations in LBE. It is important that the boundary conditions applied for the simulation represent the correct physical problem. In cavity simulations, for example, besides the uniform top velocity and no-slip conditions on the walls, the mass must be conserved globally. Any violation of this restriction will produce nonphysical results. It is found in our computational experiments (not presented in this paper) that some improper boundary conditions can give a qualitatively reasonable flow but lead to quantitatively incorrect results.

2. A range of parameters for the model is explored for the cavity simulations. Parameters such as the lattice size, maximum velocity, the ratio of rest and moving particles, and the single relaxation time are adjustable in the LBE. The lattice size should be chosen so that adequate resolution for all scales in the problem can be obtained at an affordable cost. The maximum velocity used in a simulation should be sufficiently small, inducing small compressibility errors, and consistent with the equilibrium distribution which is an expansion of small velocity. For the Chapman–Enskog expansion to be valid, the spatial gradients of density and velocity should be small also. Since the maximum velocity and lattice size are limited, the single relaxation time needs to be small to achieve the higher Reynolds numbers. It is found that the lowest relaxation time leading to stable simulations depends on the ratio of rest and moving particles, on the maximum velocity and on the problem. To obtain a reliable simulation, the relaxation time τ should be chosen not too close to the lowest limit for the problem under investigation. It cannot be smaller than $\frac{1}{2}$ to ensure positive viscosity, in any case. On the other hand, since the speed of sound in the LBE is of order one, and the relaxation time represents characteristic collision time; hence, τ has the same order as the mean free path (measured in lattice units). Therefore, τ should not be too large to guarantee that the mean free path is much smaller than the physical characteristic length scale. This is a necessary condition for the microscopic statistics of the LBE to approach the Navier–Stokes equations as shown in the multiscale expansion (see the Appendix).

3. The compressibility effect may become important when physical quantities of the smallest scale in an incompressible flow is comparable to the compressibility error. Using a smaller maximum velocity can reduce this error. However, it is not practical to predict scales on the order of 10^{-8} or smaller by the present LBE method.

4. The square lattice is better than the triangular lattice (FHP) in two-dimensional simulations because the former can reach higher values of Re number for the same lattice size and maximum velocity.

5. The computer time used in the simulations is not compared carefully with other methods, since the LBE includes transient effects in this problem and, hence, is not economical, compared with the multigrid method. There is no doubt, however, that the method can simulate unsteady and other complex problems on a parallel computer [4, 5, 15–33].

6. There are some ripples in the streamline, vorticity, and pressure contour plots for high Re. The authors tried to eliminate these ripples by subgrid modeling [49], but they were not successful. The wiggles appear mostly in the two upper corners, where singularity causes high gradients on the vorticity and pressure. The wiggles are also seen in the lower right corner of the tertiary vortex on the streamline plot for Re = 7500. By carefully examining the plots for Re = 7500, one can find that the wiggles clearly are aligned with lattice directions. Hence, it is suspected that the lattice effects due to the discreteness of the velocity are the main cause of the wiggles. It is still an open question how to reduce the oscillation of the solution for high values of Re.

Lattice gas and lattice Boltzmann methods are relatively new approaches for simulating complex flows. It is apparent that further research on both theoretical and practical aspects is needed. Implementation of higher order boundary conditions, models for better resolving small scale phenomena, applications in new fields, improvement of thermodynamical models, and careful studies for three-dimensional geometries are challenges for future research.

APPENDIX

This appendix details the derivation that shows how the Navier–Stokes equations are recovered from a lattice Boltzmann equation on a square lattice by using the Chapman–Enskog expansion procedure of kinetic theory. In addition, the equilibrium distribution functions are obtained to guarantee that the requirements of isotropy, Galilean-invariance, and velocity-independent pressure are satisfied.

On each node of a square lattice there are three types of particle, namely, a rest particle, a particle moving along perpendicular directions, and a moving particle along diagonal directions (see Fig. A1).

The velocity vectors $\mathbf{e}_{1i}$, $\mathbf{e}_{2i}$ are defined as

$$\mathbf{e}_{1i} = \left(\cos\frac{i-1}{2}\pi, \sin\frac{i-1}{2}\pi\right), \quad i = 1, ..., 4,$$

$$\mathbf{e}_{2i} = \sqrt{2}\left(\cos\left(\frac{i-1}{2}\pi + \frac{\pi}{4}\right), \sin\left(\frac{i-1}{2}\pi + \frac{\pi}{4}\right)\right),$$

$$i = 1, ..., 4.$$

The symmetric properties of the tensor $\sum_i (e_{\sigma i\alpha} e_{\sigma i\beta} \cdots)$ (where $\alpha, \beta, ... = 1$ or 2 denote the components of $\mathbf{e}_{\sigma i}$) are needed in the derivation and given as follows:

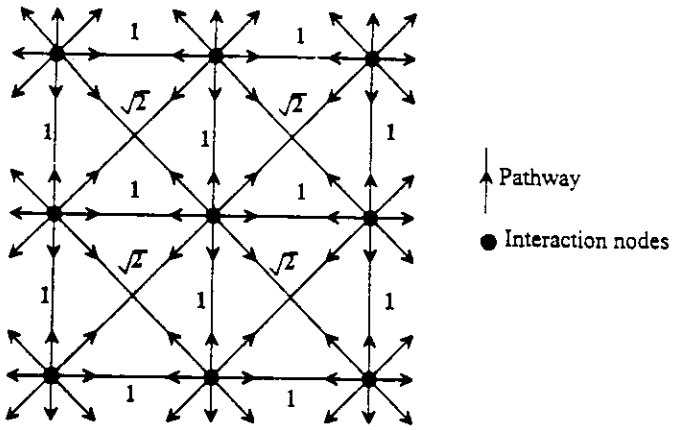

FIG. A1. Schematic of a square lattice.

The odd orders of the tensor are equal to zero. The second-order tensor satisfies

$$\sum_i e_{\sigma i\alpha} e_{\sigma i\beta} = 2e_\sigma^2 \delta_{\alpha\beta}, \quad \alpha, \beta = 1, 2, \tag{1}$$

where $\delta_{\alpha\beta}$ is the Kronecker delta and $e_1 = 1$, $e_2 = \sqrt{2}$ are the lengths of $\mathbf{e}_{1i}$ and $\mathbf{e}_{2i}$, respectively.

Finally, the fourth-order tensor has an expression as

$$\sum_i e_{\sigma i\alpha} e_{\sigma i\beta} e_{\sigma i\gamma} e_{\sigma i\theta} = \begin{cases} 2\delta_{\alpha\beta\gamma\theta}, & \sigma = 1, \\ 4\Delta_{\alpha\beta\gamma\theta} - 8\delta_{\alpha\beta\gamma\theta}, & \sigma = 2, \end{cases} \tag{2}$$

where $\delta_{\alpha\beta\gamma\theta} = 1$ for $\alpha = \beta = \gamma = \theta$, and 0 otherwise, $\Delta_{\alpha\beta\gamma\theta} = (\delta_{\alpha\beta}\delta_{\gamma\theta} + \delta_{\alpha\gamma}\delta_{\beta\theta} + \delta_{\alpha\theta}\delta_{\beta\gamma})$.

The Chapman–Enskog procedure is an asymptotic expansion method for solving the Boltzmann equation in kinetic theory. It uses a small Knudsen number (the ratio of the mean free path to the characteristic flow length) in an asymptotic expansion. The lattice unit is required to be small, compared with the macroscopic characteristic scale. Using δ as the small lattice time unit in physical unit, the lattice Boltzmann BGK equation in physical units is

$$f_{\sigma i}(\mathbf{x} + \delta\mathbf{e}_{\sigma i}, t + \delta) - f_{\sigma i}(\mathbf{x}, t) = -\frac{1}{\tau}[f_{\sigma i}(\mathbf{x}, t) - f_{\sigma i}^{(0)}(\mathbf{x}, t)]. \tag{3}$$

A general form of $f_{\sigma i}^{(0)}(\mathbf{x}, t)$ can be taken as

$$f_{\sigma i}^{(0)}(\mathbf{x}, t) = A_\sigma + B_\sigma(\mathbf{e}_{\sigma i}\cdot\mathbf{u}) + C_\sigma(\mathbf{e}_{\sigma i}\cdot\mathbf{u})^2 + D_\sigma u^2. \tag{4}$$

Here A_σ, B_σ, C_σ, and D_σ are coefficients to be determined which depend on ρ, but not on u. Equation (4) can be thought as a special type of small velocity (up to the u^2 term) expansion of $f_{\sigma i}^{(0)}$. It is obvious that $B_0 = C_0 = 0$.

Taylor expanding Eq. (3) and retaining terms up to $O(\delta^2)$ results in

$$\delta\left[\frac{\partial}{\partial t} + (\mathbf{e}_{\sigma i}\cdot\nabla)\right] f_{\sigma i} + \frac{\delta^2}{2}\left[\frac{\partial}{\partial t} + (\mathbf{e}_{\sigma i}\cdot\nabla)\right]^2 f_{\sigma i} + O(\delta^3) = -\frac{1}{\tau}[f_{\sigma i}(\mathbf{x}, t) - f_{\sigma i}^{(0)}(\mathbf{x}, t)]. \tag{5}$$

Next, the Chapman–Enskog-like expansion is applied to Eq. (5). As discussed in the conclusion, the value of parameter τ (in lattice units) should be about the same order as the mean free path; hence, $\tau\delta$ is about equal to the value of the mean free path in physical units. Under the assumption that mean free path is of the same order of δ (or τ is of order one), δ can play the role of the Knudsen number. It is possible, however, that τ can be larger than order one. Then the procedure needs to be modified and the expression of viscosity will be slightly different from the expression given below. Expanding $f_{\sigma i}$ about $f_{\sigma i}^{(0)}$,

$$f_{\sigma i} = f_{\sigma i}^{(0)} + \delta f_{\sigma i}^{(1)} + \delta^2 f_{\sigma i}^{(2)} + O(\delta^3) \tag{6}$$

with conservation laws $\sum_\sigma \sum_i f_{\sigma i}^{(0)} = \rho$, $\sum_\sigma \sum_i f_{\sigma i}^{(0)} \mathbf{e}_{\sigma i} = \rho\mathbf{u}$ and constraints $\sum_\sigma \sum_i f_{\sigma i}^{(n)} = 0$ and $\sum_\sigma \sum_i f_{\sigma i}^{(n)} \mathbf{e}_{\sigma i} = 0$ for $n \geq 1$. These constraints imply that the non-equilibrium distributions do not contribute to the local values of density and momentum. These give constraints for coefficients A_σ, B_σ, C_σ, and D_σ as

$$A_0 + 4A_1 + 4A_2 = \rho, \tag{7}$$

$$2C_1 + 4C_2 + D_0 + 4D_1 + 4D_2 = 0, \tag{8}$$

and

$$2B_1 + 4B_2 = \rho. \tag{9}$$

To discuss changes in different time scales, t_0 and t_1 are introduced as $t_0 = t$, $t_1 = \delta t$, ...; thus

$$\frac{\partial}{\partial t} = \frac{\partial}{\partial t_0} + \delta\frac{\partial}{\partial t_1} + \cdots. \tag{10}$$

Substituting Eqs. (6) and (10) into Eq. (5), the equation to order of δ is

$$(\partial_{t_0} + \mathbf{e}_{\sigma i}\cdot\nabla) f_{\sigma i}^{(0)} = -\frac{1}{\tau} f_{\sigma i}^{(1)}. \tag{11}$$

The equation to order δ^2 is simplified by using Eq. (11):

$$\partial_{t_1} f_{\sigma i}^{(0)} + (\partial_{t_0} + \mathbf{e}_{\sigma i}\cdot\nabla)\left(1 - \frac{1}{2\tau}\right) f_{\sigma i}^{(1)} = -\frac{1}{\tau} f_{\sigma i}^{(2)}. \tag{12}$$

To derive the equations for ρ and $\rho\mathbf{u}$ to first order in δ, a summation of Eq. (11) with respect to σ and i is taken to give the first-order continuity equation

$$\partial_{t_0}\rho + \nabla\cdot(\rho\mathbf{u}) = 0. \tag{13}$$

Similarly, multiplying by $\mathbf{e}_{\sigma i}$ in Eq. (11) and taking the summation as above gives

$$\partial_{t_0}(\rho\mathbf{u}) + \nabla\cdot\Pi^{(0)} = 0, \tag{14}$$

where $\Pi = \sum_\sigma \sum_i (\mathbf{e}_{\sigma i}\mathbf{e}_{\sigma i})f_{\sigma i}$ is the momentum flux tensor. Similarly, the equations of order of δ^2 for ρ and $\mathbf{u}$ can be obtained from Eq. (12) as

$$\partial_{t_1}\rho = 0, \tag{15}$$

$$\partial_{t_1}(\rho\mathbf{u}) + \nabla\cdot\left(1 - \frac{1}{2\tau}\right)\Pi^{(1)} = 0. \tag{16}$$

Substituting the expression of equilibrium distribution, $\Pi^{(0)}$ can be written as

$$\begin{aligned}\Pi^{(0)}_{\alpha\beta} = {} & [2A_1 + 4A_2 + (4C_2 + 2D_1 + 4D_2)u^2]\delta_{\alpha\beta} \\ & + 8C_2u_\alpha u_\beta + (2C_1 - 8C_2)u_\alpha u_\beta\delta_{\alpha\beta}.\end{aligned} \tag{17}$$

The first term is the pressure term and the other two are nonlinear terms. In order to obtain a velocity-independent pressure, the coefficient of u^2 is chosen to satisfy

$$4C_2 + 2D_1 + 4D_2 = 0. \tag{18}$$

To have Galilean invariance, the non-isotropic term is eliminated by choosing

$$2C_1 - 8C_2 = 0. \tag{19}$$

Equation (17) becomes

$$\Pi^{(0)}_{\alpha\beta} = (2A_1 + 4A_2)\delta_{\alpha\beta} + 8C_2u_\alpha u_\beta. \tag{20}$$

Assuming that

$$8C_2 = \rho \tag{21}$$

and

$$2A_1 + 4A_2 = c_s^2\rho, \tag{22}$$

where c_s is speed of sound, gives the final expression for $\pi^{(0)}$ as

$$\Pi^{(0)}_{\alpha\beta} = c_s^2\rho\delta_{\alpha\beta} + \rho u_\alpha u_\beta. \tag{23}$$

Substituting Eq. (23) into Eq. (14) results in

$$\partial_{t_0}(\rho\mathbf{u}) + \nabla\cdot(\rho\mathbf{u}\mathbf{u}) = -\nabla(c_s^2\rho). \tag{24}$$

Equations (13) and (24) are Euler equations that are derived from the δ-order of the expansion of the lattice Boltzmann equation. The pressure is given by $p = c_s^2\rho$.

To derive the equations accurate to δ^2, the quantity $\nabla\cdot\Pi^{(1)}$ needs to be evaluated. Substituting the non-equilibrium distribution expressed in Eq. (11) into $\Pi^{(1)}_{\alpha\beta}$ and using Eq. (13) and Eq. (23) leads to

$$\begin{aligned}\Pi^{(1)}_{\alpha\beta} = {} & -\tau\{\partial_{t_0}[(c_s^2\rho)\delta_{\alpha\beta} + \rho u_\alpha u_\beta] + \partial_\gamma B_1 u_\theta 2\delta_{\alpha\beta\gamma\theta} \\ & + \partial_\gamma B_2 u_\theta(4\Delta_{\alpha\beta\gamma\theta} - 8\delta_{\alpha\beta\gamma\theta})\} \\ = {} & -\tau\{-c_s^2\delta_{\alpha\beta}\partial_\gamma(\rho u_\gamma) + \partial_{t_0}(\rho u_\alpha u_\beta) + \partial_\alpha(2B_1 - 8B_2)u_\beta\delta_{\alpha\beta} \\ & + 4\partial_\gamma(B_2u_\gamma)\delta_{\alpha\beta} + 4\partial_\alpha(B_2u_\beta) + 4\partial_\beta(B_2u_\alpha)\},\end{aligned} \tag{25}$$

where the Einstein summation convention is used. To maintain isotropy, set

$$2B_1 - 8B_2 = 0. \tag{26}$$

Recalling Eq. (9), B_1 and B_2 can be uniquely determined as

$$B_2 = \frac{\rho}{12}, \quad B_1 = \frac{\rho}{3}. \tag{27}$$

Therefore, Eq. (25) can be written as

$$\begin{aligned}\Pi^{(1)}_{\alpha\beta} = {} & -\tau\{\tfrac{1}{3}\partial_\gamma(\rho u_\gamma)\delta_{\alpha\beta} + \tfrac{1}{3}\partial_\alpha(\rho u_\beta) + \tfrac{1}{3}\partial_\beta(\rho u_\alpha) \\ & - c_s^2\partial_\gamma(\rho u_\gamma)\delta_{\alpha\beta} + \partial_{t_0}(\rho u_\alpha u_\beta)\}.\end{aligned} \tag{28}$$

The last term can be simplified using Eq. (24) to take the form

$$\partial_{t_0}(\rho u_\alpha u_\beta) = -u_\alpha\partial_\beta(c_s^2\rho) - u_\beta\partial_\alpha(c_s^2\rho) - \partial_\gamma(\rho u_\alpha u_\beta u_\gamma), \tag{29}$$

Eq. (28) therefore becomes

$$\begin{aligned}\Pi^{(1)}_{\alpha\beta} = {} & -\tau\{(\tfrac{1}{3} - c_s^2)\partial_\gamma(\rho u_\gamma)\delta_{\alpha\beta} + \tfrac{1}{3}\partial_\alpha(\rho u_\beta) + \tfrac{1}{3}\partial_\beta(\rho u_\alpha) \\ & - u_\alpha\partial_\beta(c_s^2\rho) - u_\beta\partial_\alpha(c_s^2\rho) - \partial_\gamma(\rho u_\alpha u_\beta u_\gamma)\}.\end{aligned} \tag{30}$$

Combining equations of $O(\delta)$ and $O(\delta^2)$ for ρ and $\mathbf{u}$, and Eqs. (13), (24), (15), and (16) with Eq. (30) gives the correct form of the continuity equation (with an error term $O(\delta^2)$ being omitted),

$$\partial_t \rho + \nabla \cdot (\rho \mathbf{u}) = 0, \tag{31}$$

and the momentum equation may be written in the form

$$\begin{aligned} \partial_t(\rho u_\alpha) + \partial_\beta(\rho u_\alpha u_\beta) = & -\partial_\alpha(c_s^2 \rho) \\ & + \delta\{\partial_\alpha[(\tau - \tfrac{1}{2})(\tfrac{1}{3} - c_s^2)\partial_\gamma(\rho u_\gamma)] \\ & + \partial_\beta(\tau - \tfrac{1}{2})[\tfrac{1}{3}\rho(\partial_\alpha u_\beta + \partial_\beta u_\alpha) \\ & + (\tfrac{1}{3} - c_s^2)(u_\alpha \partial_\beta \rho + u_\beta \partial_\alpha \rho) \\ & - \partial_\gamma(\rho u_\alpha u_\beta u_\gamma)]\} + O(\delta^2). \end{aligned} \tag{32}$$

Consider the constraints on A_σ given in Eqs. (7) and (22) and choose

$$A_0 = \tfrac{4}{9}\rho, \quad A_1 = \tfrac{1}{9}\rho, \quad A_2 = \tfrac{1}{36}\rho,$$

then Eq. (7) is satisfied and the sound speed is given by

$$c_s^2 = \tfrac{1}{3}.$$

Equation (32) is simplified as

$$\begin{aligned} \partial_t(\rho u_\alpha) + \partial_\beta(\rho u_\alpha u_\beta) = & -\partial_\alpha(c_s^2 \rho) + \partial_\beta(2\nu\rho S_{\alpha\beta}) \\ & - \delta\partial_\beta(\tau - \tfrac{1}{2})\partial_\gamma(\rho u_\alpha u_\beta u_\gamma) + O(\delta^2), \end{aligned} \tag{33}$$

where $S_{\alpha\beta} = \frac{1}{2}(\partial_\alpha u_\beta + \partial_\beta u_\alpha)$ is the stain-rate tensor, $p = c_s^2 \rho$, and

$$\nu = \frac{2\tau - 1}{6}\delta, \tag{34}$$

with ν being the kinematic viscosity, now measured in physical units. Re is computed using $\mathrm{Re} = UL/\nu$, where L is the characteristic length in physical units. If this equation is written in lattice units, δ will not appear explicitly in the equation. The third term on the right is the nonlinear deviation term of the incompressible flow [51]. Recall the Navier–Stokes equations in two dimensions [50],

$$\partial_t(\rho u_\alpha) + \partial_\beta(\rho u_\alpha u_\beta) = -\partial_\alpha p + \partial_\beta\{2\mu(S_{\alpha\beta} - \tfrac{1}{2}u_{\gamma\gamma}\delta_{\alpha\beta})\}, \tag{35}$$

and

$$\partial_t \rho + \nabla \cdot (\rho \mathbf{u}) = 0. \tag{36}$$

For an incompressible fluid, the Navier–Stokes equations become

$$\partial_t(\rho u_\alpha) + \partial_\beta(\rho u_\alpha u_\beta) = -\partial_\alpha p + \partial_\beta\{2\mu S_{\alpha\beta}\}. \tag{37}$$

$$\nabla \cdot \mathbf{u} = 0 \tag{38}$$

It is seen that Eq. (33) is exactly the same as the incompressible Navier-Stokes equation (37), omitting the $O(\delta u^3)$ and $O(\delta^2)$ in Eq. (33), while Eq. (31) approximates Eq. (38) neglecting changes of ρ.

The remaining coefficients D_0, D_1, and D_2 are related by Eq. (8) and Eq. (18), so there is one free parameter. Since all coefficients of particle 2 are one-fourth of the corresponding coefficients of particle 1, one can require $D_1 = 4D_2$. Hence, the remaining coefficients are determined:

$$D_0 = -\tfrac{2}{3}\rho, \quad D_1 = -\tfrac{1}{6}\rho, \quad D_2 = -\tfrac{1}{24}\rho.$$

Finally, the equilibrium distribution functions are given by Eq. (5) in Section 2.

ACKNOWLEDGMENTS

Discussions with Li-shi Luo, Daryl Grunau, Xiaowen Shan, Jim Sterling, Yue Hong Qian, Hu Dong Chen, Balu Nadiga, and Norman Zabusky are appreciated. This work is supported by the Department of Energy at Los Alamos National laboratory. The authors wish to acknowledge the Advanced Computing Laboratory of Los Alamos National Laboratory for providing use of the connection machines, CM-200 and CM-5. Hou and Cogley from Kansas State University gratefully appreciate support from IBM, the National Science Foundation (Grant DDM-9113780), and the Kansas Space Grant Consortium.

REFERENCES

1. U. Frisch, B. Hasslacher, and Y. Pomeau, *Phys. Rev. Lett.* **56,** 1505 (1986).
2. U. Frisch, D. d'Humières, B. Hasslacher, P. Lallemand, Y. Pomeau, and J.-P. Rivet, *Complex Systems* **1,** 649 (1987).
3. S. Wolfram, *J. Statist. Phys.* **45,** 471 (1986).
4. G. D. Doolen (Ed.), *Lattice Gas Methods for Partial Differential Equations* (Addison–Wesley, Reading, MA, 1989).
5. G. D. Doolen (Ed.), *Lattice Gas Methods: Theory, Applications and Hardware,* Physica D, Vol. 47 (North Holland, Amsterdam, 1991).
6. G. McNamara and G. Zanetti, *Phys. Rev. Lett.* **61,** 2332 (1988).
7. F. Higuera and J. Jimenez, *Europhys. Lett.* **9,** 663 (1989).
8. F. Higuera and S. Succi, *Europhys. Lett.* **8,** 517 (1989).
9. Y. Qian, Ph.D. thesis, de l'Universit é Pierre et Marie Curie, January 1990.
10. S. Chen, H. Chen, D. Martinez, and W. H. Matthaeus, *Phys. Rev. Lett.* **67,** 3776 (1991).
11. Y. Qian, D. d'Humières, and P. Lallemand, *Europhys. Lett.* **17**(6), 479 (1992).
12. H. Chen, S. Chen, and W. H. Matthaeus, *Phys. Rev. A* **45,** 5339 (1992).
13. R. D. Kingdon, P. Schofield, and L. White, *J. Phys. A: Math. Gen.* **25,** 3559 (1992).
14. P. L. Bhatnagar, E. P. Gross, and M. Krook, *Phys. Rev.* **94,** 511 (1954).
15. S. Succi, R. Benzi, and F. Higuera, *Physica D* **47,** 219 (1991).
16. S. Chen, Z. Wang, X. Shan, and G. D. Doolen, *J. Statist. Phys.* **68,** 379 (1992).
17. G. McNamara and B. Alder, "Lattice Boltzmann Simulation of High Reynolds Number Fluid Flow in Two dimensions," in *Microscopic Simulations of Complex Hydrodynamic Phenomena,* edited by M. Mareschal and B. L. Holien (Plenum, New York, 1992).
18. D. O. Martinez, W. H. Matthaeus, S. Chen, and D. C. Montgomery, *Phys. Fluids* **6**(3), 1285 (1994).

19. D. Rothman, *J. Geophys. Res.* **95,** 8663 (1990).
20. S. Chen, K. Diemer, G. D. Doolen, K. Eggert, C. Fu, S. Gutman, and B. J. Travis, *Physica D* **47,** 72 (1991).
21. H. Chen and W. H. Matthaeus, *Phys. Rev. Lett.* **58,** 1845 (1987).
22. D. O. Martinez, S. Chen, and W. H. Matthaeus, *Phys. Plasmas* **1**(6) (1994).
23. D. Rothman and J. M. Keller, *J. Statist. Phys.* **52,** 1119 (1988).
24. J. A. Somers and P. Rem, *Physica D* **47,** 39 (1991).
25. D. Grunau, S. Chen, and K. Eggert, *Phys. Fluids A* **5,** 2557 (1993).
26. X. Shan and H. Chen, *Phys. Rev. E* **47**(3), 1815 (1993).
27. D. Dab, A. Lawniczak, J.-P. Boon, and R. Kapral, *Phys. Rev. Lett.* **64,** 2462 (1990).
28. R. Kapral, A. Lawniczak, and P. Masiar, *Phys. Rev. Lett.* **66,** 2539 (1991).
29. S. Ponce Dawson, S. Chen, and G. D. Doolen, *J. Chem. Phys.* **98,** 1514 (1993).
30. R. Monaco (Ed.), *Discrete Kinetic Theory, Lattice Gas Dynamics and Foundations of Hydrodynamics* (World Scientific, Singapore, 1989).
31. J. P. Boon (Ed.), *J. Statist. Phys.* **68**(3/4) (1992).
32. D. Rothman and S. Zaleski, *Rev. Modern Phys.* **66,** 1417 (1994).
33. M. B. Reider and J. D. Sterling, in *Comput. & Fluids,* in press.
34. O. Burggraf, *J. Fluid Mech.* **24,** 113 (1966).
35. F. Pan and A. Acrivos, *J. Fluid Mech.* **28,** 643 (1967).
36. J. D. Bozeman and C. Dalton, *J. Comput. Phys.* **12,** 348 (1973).
37. A. S. Benjamin and V. E. Denny, *J. Comput. Phys.* **33,** 340 (1979).
38. U. Ghia, K. N. Ghia, and C. Y. Shin, *J. Comput. Phys.* **48,** 387 (1982).
39. R. Schreiber and H. B. Keller, *J. Comput. Phys.* **49,** 310 (1983).
40. S. P. Vanka, *J. Comput. Phys.* **65,** 138 (1986).
41. P. Demaret and M. O. Deville, *J. Comput. Phys.* **95,** 359 (1991).
42. G. K. Batchelor, *J. Fluid Mech.* **1,** 177 (1956).
43. J. L. Sohn, *Int. J. Numer. Methods Fluids* **8,** 1469 (1988).
44. P. A. Skordos, *Phys. Rev. E* **48,** 6 (1993).
45. D. P. Ziegler, *J. Statist. Phys.* **71**(5/6) (1993).
46. K. Atkinson, *Elementary Numerical Analysis,* 2nd ed. (Wiley, New York, 1993), p. 173.
47. Q. Zou, S. Hou, S. Chen, and G. D. Doolen, submitted.
48. J. D. Sterling and S. Chen, *J. Comput. Phys.*, in press.
49. S. Hou, J. D. Sterling, S. Chen, and G. D. Doolen, *The Fields Institute Communications Series,* in press.
50. G. K. Batchelor, *Introduction to Fluid Dynamics,* (Cambridge University Press, Cambridge, 1967), p. 147.
51. Y. H. Qian and S. A. Orszag, *Europhys. Lett.* **21**(3), 255 (1993).